Received: 8 April 2021 | Revised: 23 August 2021 | Accepted: 2 September 2021

DOI: 10.1002/fuce.202100035

Fuel Cells
From Fundamentals to Systems

ORIGINAL RESEARCH PAPER

# An experimental and numerical study of the exchange current density in an HTPEM fuel cell

**Murat Çelik**[1] | **Gülşah Elden**[2]

[1] Department of Mechanical Engineering, Abdullah Gul University, Kocasinan, Kayseri, Turkey

[2] Department of Energy Systems Engineering, Erciyes University, Melikgazi, Kayseri, Turkey

Correspondence
Gülşah Elden, Erciyes University, Department of Energy Systems Engineering, Melikgazi, 38039 Kayseri, Turkey.
E-mail: gulsah@erciyes.edu.tr

**Abstract**

The purpose of this study is to examine the effects of exchange current density, as dependent on operating parameters, on the activation polarization in an HTPEM fuel cell. In line with this purpose, cell performance tests were performed for different relative humidity levels (from 0 to 20% in steps of 5%) and six different acid doping levels (4.26, 4.53, 4.95, 5.51, 7.24, 7.51 $H_3PO_4$/RPU PBI) at constant cell temperature (120 °C). The exchange current densities, as dependent on acid doping level and relative humidity, were determined by fitting a zero-dimensional steady-state mathematical model to the cell performance test results. Finally, to investigate the activation polarization in the cell, the exchange current densities obtained were incorporated within a numerical model. The results show that the effects of relative humidity on the exchange current density are relatively limited at all acid doping levels when the relative humidity is greater than 5%. The exchange current densities exhibit a decreasing trend with increasing acid doping level. Furthermore, it was found that the acid doping level and relative humidity have a strong influence on the anode overpotential, whereas no significant effect on the cathode overpotential was observed.

**KEYWORDS**

acid doping level, relative humidity, exchange current density, activation polarization, high temperature PEM fuel cell

## 1 | INTRODUCTION

The need for clean and highly efficient energy technologies has recently begun to rise due to increased greenhouse gas emissions. Fuel cells are clean, efficient, and renewable energy conversion devices that convert chemical energy (e.g., hydrogen) directly into electrical energy. One of the most widespread fuel cell types used as a power source is proton exchange membrane fuel cells (PEM-FCs). PEM-FCs are used in portable, transportation, and stationary applications since they can operate over a wide temperature range (80 °C–200 °C) and at different relative humidities (0%–100%) depending on the membrane material. It is possible to reach high temperatures (up to 200 °C) in PEM-FCs using polybenzimidazole (PBI) membranes that are non-perfluorinated materials with excellent mechanical strengths, and high chemical and thermal stabilities at high temperatures.

The proton conductivity of PBI in pure form is quite low ($10^{-10}$ S $m^{-1}$). Therefore, PBI membranes are doped with different acids such as phosphoric acid ($H_3PO_4$), sulphuric acid ($H_2SO_4$), or hydrobromic acid (HBr) in order to increase proton conductivity [1]. For high-temperature PEM-FCs, it is known from the literature

  

that the cell temperature and relative humidity have a positive effect on the proton conductivity and cell performance. Even though PBI-based PEM-FCs usually operate under conditions of zero humidity, their performance is significantly influenced by increasing relative humidity due to enhanced proton conductivity [2–5]. He [3] demonstrated that the proton conductivity of PBI or acid-doped PBI membranes increases with increasing relative humidity. In their study, when relative humidity was increased from 5% to 20%, the proton conductivity of the PBI membrane at 140 °C increased from 0.035 S $cm^{-1}$ to 0.046 S $cm^{-1}$. The proton conductivity increase at 200 °C was much greater than that at 140 °C. Asensio et al. [4] examined whether the proton conductivity of PBI-based membranes increases with increasing relative humidity between 50 °C and 180 °C. Similarly, Ma et al. [5] concluded that an increased relative humidity has a positive effect on proton conductivity in the temperature range 120 °C to 160 °C. Modeling and simulation techniques have been used to better understand mass/charge transfer and electrochemical phenomena and to estimate cell performance in fuel cell systems. Electrochemical phenomena are generally modeled via the Butler-Volmer equation, one of the key parameters of which is the exchange current density, which is a measure of electrode effectiveness. The challenges to determining the exchange current density itself, and indeed, the influence of other parameters on it, are substantial, particularly with regard to modeling the PEM-FCs to gain an insight into the electrode kinetics. Sun et al. [6] obtained a value of 27.2 mA $cm^{-2}$ for the exchange current density with the rotating disc electrode (RDE) method in hydrogen oxidation reactions of Pt particles varying between 2.1 and 2.5 nm in size. In another study by Tang et al. [7], the RDE method was used to test the validity of a newly derived equation to calculate exchange current density. Neyerlin et al. [8] determined the exchange current densities for the electrodes of a PEM fuel cell that were loaded with amounts of Pt as low as 0.003 mg $cm^{-2}$. Liu et al. [9] presented an extensive study of oxygen reduction reactions at Pt interfacing $H_3PO_4$-doped PBI. They examined the effects of $H_3PO_4$ and $H_2O$ content on the exchange current density. Zhang et al. [10] expressed the relationship between exchange current density and relative humidity mathematically, and further determined the effects of relative humidity on the activation polarization. Statistical methods are also frequently used for parameter estimation purposes. Haji [11] determined the exchange current density in a Nafion-based PEM fuel cell via multiple non-linear regression. The exchange current density varies between $3.5 \times 10^{-5}$ and $1.6 \times 10^{-4}$ A $cm^{-2}$ for temperatures between 25 and 45 °C. By fitting a model equation including all losses in a fuel cell into experimental polarization data, parameters such as the charge transfer coefficient and internal resistance can also be estimated. Similarly, exchange current densities in PEM fuel cells have been estimated through regression approaches by Ubeda et al. and Santarelli et al. [12, 13].

Being a measure of charge transfer [14], it has been shown that exchange current density plays a major role in the activation overpotential and overall cell performance. Carnes and Djilali [15] showed that cathode exchange current density significantly affects cell performance, especially for the low current densities. As expected, their results suggested that higher exchange current densities yield lower overpotentials for both anode and cathode, though that for the cathode overpotential is somewhat greater than for the anode. Similarly, Min et al. [16] published a sensitivity analysis of the parameters affecting the performance of a PEM fuel cell using extensive simulations. They pointed out the significance of the exchange current density multiplied by the specific area of the cathode side of the cell and its influence over the polarization curve. Iranzo et al. [17] used exchange current density to calibrate their model results using experimental results. A sensitivity analysis carried out by Zhao et al. [18] reiterates the effect of exchange current densities on the voltage deviation of the cell by varying the values of two empirical parameters used in an Arrhenius-type equation that relates the exchange current density to temperature, pressure, and activation energy. Arif et al. [19] investigated the influences of a variety of parameters such as exchange current density and contact resistance on the overpotentials in a PEM fuel cell. It was shown that the exchange current density and charge transfer coefficient are principally responsible for the magnitude of the activation overpotential. They emphasized the fact that a higher exchange current density leads to a lower activation potential and thus increased overall performance. Zhang et al. [20] pointed out the relationship between oxygen concentration and activation losses in a PEM fuel cell. They concluded that in the cell regions with low oxygen concentrations, the activation losses are the largest.

Most of the studies related to the exchange current density are on Nafion-based PEM fuel cells. To the best of our knowledge, there is no study that directly investigates the effects of operating parameters such as acid doping and relative humidity on the exchange current density at a constant cell temperature in a PBI-based PEM fuel cell. Accordingly, in this study the effects of these parameters on the exchange current density in a PBI-based high-temperature PEM fuel cell are investigated experimentally. Furthermore, a numerical study is performed to determine the effects of the exchange current density on the activation polarization in a high temperature PEM fuel cell.

**TABLE 1** Properties of the PBI membrane

| The molecular weight of the repeating unit | 308 g $mol^{-1}$ |
|---|---|
| Density | 1.3 g $cc^{-1}$ |
| Glass transition temperature | 427 °C |
| Tear strength | 1.47 lb $mil^{-1}$ (23 °C) |
| Membrane thickness | 55 $\mu$m |

**TABLE 2** Acid doping levels of the membranes for each phosphoric acid concentration

| $H_3PO_4$ concentrations | Acid doping level |
|---|---|
| 11 M | 4.26 |
| 12 M | 4.53 |
| 13 M | 4.95 |
| 14 M | 5.51 |
| 15 M | 7.24 |
| 16 M | 7.51 |

## 2 | MATERIALS AND METHODS

### 2.1 | Experimental study

#### 2.1.1 | Preparation of membrane electrode assembly

The first objective of this study is to determine the exchange current density depending on the acid doping level and relative humidity at a constant cell temperature in a $H_3PO_4$-doped PBI polymer electrolyte membrane fuel cell. In line with this objective, PBI membranes were doped with $H_3PO_4$ to different levels. Some properties of the PBI films used are reported in Table 1. PBI films (PBI Performance Products, Inc.) were separately doped by immersing into orthophosphoric acid (85 wt.%) at concentrations varying from 11 to 16 M for 6 h at 120 °C. Membranes were subsequently kept at 110 °C for 24 h to ensure the removal of water. The phosphoric acid doping levels of the prepared membranes were calculated using Eq. (1) [13].

$$X = \frac{W_1 - W_0}{W_0} \cdot \frac{308\ \text{g PBI/RU of PBI}}{98\ g\ H_3PO_4/mol\ H_3PO_4} \quad (1)$$

where $W_1$ and $W_0$ are the final and initial weight of the membrane samples, respectively. The acid doping levels of the membranes for each phosphoric acid concentration are given in Table 2.

In order to prepare the membrane electrolyte assembly (MEA), doped membrane samples were hot pressed between two gas diffusion electrodes (GDE) for 10 min at 135 °C and 25 bar. The Nafion ionomer content of the GDEs was 25 wt.% and the platinum loadings were 0.4 mg $cm^{-2}$ for both anode and cathode sides. The active area of the MEAs was 25 $cm^2$.

#### 2.1.2 | Performance tests of the single cell

The single test cell used in the experiments consisted of nine layers including two graphite bipolar plates with four serpentine channels, two current collectors, two viton gaskets to provide sealing and prevent electrical short circuits, two endplates, and the in-house MEA. These layers were held together by eight bolts tightened to a torque of 2.8 N m, which was applied to each bolt separately. The cell temperature was controlled by embedded electrical heaters and thermocouples within the graphite plates. High purity $H_2$ and $O_2$, as the fuel and oxidant, were fed to the anode and the cathode at 20 psi with flow rates of 0.05 slpm and 0.6 slpm, respectively. The inlet gases were passed through bubble humidifiers to reach the desired relative humidity. In order to prevent gas leakage into the test cell, it was purged with nitrogen gas prior to the cell performance tests. The cell was maintained at 0.6 V until steady performance was achieved. Polarization curves were then obtained by decreasing the voltage from the open-circuit voltage to 0.4 V in steps of 20 mV using a potentiostat/galvanostat.

### 2.2 | Numerical study

#### 2.2.1 | Mathematical model

One of the more important losses affecting fuel cell performance is activation polarization. Activation polarization losses, which occur at both the anode and cathode, are influenced by reaction mechanism, catalyst type, catalyst layer morphology, and operating parameters. These losses have a considerable influence on the exchange current density and charge transfer coefficients. Therefore, the second objective of this study is to analyze the effects of the exchange current density, which was experimentally determined based on the operating parameters, on the activation polarization losses in a high temperature PEM fuel cell. In line with this objective, a two-dimensional steady-state and single-phase model was developed using the COMSOL Multiphysics 5.5 software. Figure 5 displays the geometrical description of the two-dimensional HT-PEM fuel cell model. The computational domain was composed of the various cell components, that is, the membrane, gas diffusion layers (GDL), catalyst layers (CL), and flow channels (FC). The physical, electrochemical, and transport parameters are listed in Table 3. Some of the

**TABLE 3** The dimensions of the cell components and the transfer parameters

| Explanation and Symbol | Value | Unit |
|---|---|---|
| Channel height, Hch | $7.112 \times 10^{-3}$ | m |
| Channel width, Wch | $7.62 \times 10^{-4}$ | m |
| GDL width, Wgdl | $2 \times 10^{-4}$ | m |
| CL width, Wcl | $1 \times 10^{-5}$ | m |
| Membrane thickness, Wmembrane | $5.5 \times 10^{-5}$ | m |
| Cell temperature, Tcell | 120 | °C |
| Reference pressure, Pref | 101325 | Pa |
| Anode pressure, Pa | 137802 | Pa |
| Cathode pressure, Pc | 137802 | Pa |
| Anode viscosity, $\mu$anode | $1.19 \times 10^{-5}$ [22] | Pa s |
| Cathode viscosity, $\mu$cathode | $2.46 \times 10^{-5}$ [22] | Pa s |
| Hydrogen molar mass, $MH_2$ | 0.002 | kg $mol^{-1}$ |
| Nitrogen molar mass, $MN_2$ | 0.028 | kg $mol^{-1}$ |
| Water molar mass, $MH_2O$ | 0.018 | kg $mol^{-1}$ |
| Oxygen molar mass, $MO_2$ | 0.032 | kg $mol^{-1}$ |
| $H_2$-$H_2O$ Binary diffusion coefficient, $D_{H2\_H2O}$ | $1.5 \times 10^{-4} \cdot (T/353)^{1.5} \cdot (P_{ref}/P_a)$ | $m^2\ s^{-1}$ |
| $N_2$-$H_2O$ Binary diffusion coefficient, $D_{N2\_H2O}$ | $2.56 \times 10^{-5} \cdot T/307.15)^{1.5} \cdot (P_{ref}/P_c)$ | $m^2\ s^{-1}$ |
| $O_2$-$N_2$ Binary diffusion coefficient, $D_{O2\_N2}$ | $2.2 \times 10^{-5} \cdot (T/293.2)^{1.5} \cdot (P_{ref}/P_c)$ | $m^2\ s^{-1}$ |
| $O_2$-$H_2O$ Binary diffusion coefficient, $D_{O2\_H2O}$ | $2.82 \times 10^{-5} \cdot (T/308.1)^{1.5} \cdot (P_{ref}/P_c)$ | $m^2\ s^{-1}$ |
| Oxygen reference concentration, $C_{O2ref}$ | 17.808 | mol $m^{-3}$ |
| Hydrogen reference concentration, $C_{H2ref}$ | 66.817 | mol $m^{-3}$ |
| Electrode conductivity, $\sigma$ | 300 [23] | S $m^{-1}$ |
| GDL permeability, Kgdl | $1.76 \times 10^{-11}$ [24] | $m^2$ |
| GDL porosity, εgdl | 0.8 | |
| CL porosity, εcl | 0.3 | |
| Membrane porosity, εmembrane | 0.2 | |

assumptions underlying the model are as follows:

(i) All the reactants and water are in the gas phase and they are assumed to behave in an ideal gas.
(ii) Flow is laminar.
(iii) Porous layers are isotropic and homogenous in all directions.
(iv) The membrane is impermeable.
(v) Contact resistances at the interfaces are negligible.

The governing equations were applied individually to each component of the HT-PEM fuel cell according to the multi-domain approach. The flow of reactant and product gases in the flow channels is governed by the Navier-Stokes equation in vector form.

$$\nabla \cdot \left(\rho \vec{u}\right) = 0 \tag{2}$$

$$\nabla \cdot \left(\rho \vec{u} \otimes \vec{u} - \mu \nabla \vec{u}\right) = -\nabla\left(p + \frac{2}{3}\mu \nabla \cdot \vec{u}\right) \tag{3}$$

$$\rho \vec{u} \nabla m_i = \nabla \cdot \left[\rho m_i \sum_{j=1}^{N} D_{ij} \left\{\frac{M}{M_i}\left(\nabla m_i + m_i \frac{\nabla M}{M}\right)\right\}\right] \tag{4}$$

where $\boldsymbol{\rho}$ is the fluid density, $\boldsymbol{u}$ is the fluid velocity, $\boldsymbol{P}$ is the anode or cathode pressure, $\boldsymbol{\mu}$ is the viscosity of the fluid, $\boldsymbol{m_i}$ is the mass fraction of species $i$, $\boldsymbol{M}$ is molar mass, and $\boldsymbol{D_{ij}}$ is the temperature- and pressure-dependent Stefan-Maxwell diffusion coefficient. For both the anode and cathode sides, it is assumed that the gas mixture is well mixed and has the same temperature, pressure, and velocity in all components. The flow and mass transport in the gas diffusion layer and catalyst layer can be described via Darcy's law and the Maxwell-Stefan equation, respectively. Also, the continuity equation for both porous layers is as follows:

$$\nabla \cdot \left(\rho \varepsilon \vec{u}\right) = S_i \tag{5}$$

$$\vec{u} = -\frac{k_p}{\mu}\nabla P \tag{6}$$

$$\rho\vec{u}\nabla m_i = \nabla \cdot \left[\rho\varepsilon m_i \sum_{j=1}^{N} D_{i,j}^{eff}\left\{\frac{M}{M_i}\left(\nabla m_i + m_i\frac{\nabla M}{M}\right)\right\}\right] + S_i \tag{7}$$

where $\boldsymbol{k_p}$ is the permeability of GDL or CL, $\boldsymbol{P}$ is pressure in a porous media, $\boldsymbol{\varepsilon}$ is the porosity of the porous layers, and $\boldsymbol{D^{eff}}$ is an effective diffusion coefficient of species that are $H_2$ and $H_2O$ for the anode side and $O_2$, $N_2$, and $H_2O$ for the cathode side. The tortuosity is incorporated into the effective diffusion coefficient in a manner defined by the Bruggeman correlation.

$$D_i^{eff} = D_{ij}\varepsilon^{1.5} \tag{8}$$

Furthermore, $\boldsymbol{S_i}$ in these governing equations is a source term that accounts for only the catalyst layer. The source term, described as the mass consumption rate of reactants or the mass production rate of water, is given as follows:

$$S_{H_2} = \frac{i}{2\cdot F} \tag{9}$$

$$S_{O_2} = \frac{i}{4\cdot F} \tag{10}$$

$$S_{H_2O} = \frac{i}{2\cdot F} \tag{11}$$

As there is only water vapor transport in the $H_3PO_4$-doped PBI membrane, this transport is governed by Eqs. (12)-(13).

$$J_{H_2O} = 0 \tag{12}$$

$$J_{H_2O} = -D_{H_2O}\cdot\nabla c_{H_2O} \tag{13}$$

The charge transports in each cell component and electrochemical reaction kinetics are described via the following equations. The catalyst layers have both ionic conductivity and electrical conductivity because of a triple-phase boundary; accordingly, both ion and electron transfer in catalyst layers occur at the same time. The charge conservation equations are written separately for the anode and cathode catalyst layers as follows:

For $e^-$ (anode):

$$-\sigma_s\cdot\nabla\varphi_s = -i_a \tag{14}$$

For $H^+$ (anode);

$$-\sigma_e\cdot\nabla\varphi_e = i_a \tag{15}$$

For $e^-$ (cathode);

$$-\sigma_s\cdot\nabla\varphi_s = -i_c \tag{16}$$

For $H^+$ (cathode);

$$-\sigma_e\cdot\nabla\varphi_e = i_c \tag{17}$$

where $i_{a/c}$ is the anode or cathode current density, $\sigma_e$ is ionic conductivity and $\phi_e$ is electrolyte potential. The current densities at the anode and cathode catalyst layers can be prescribed via the Butler Volmer kinetic equation:

$$i_{a,c} = i_{0a,c}^{ref}\cdot\left(\frac{C_i}{C_i^{ref}}\right)^{\gamma}\cdot\left[\exp\left(\frac{\alpha_a\cdot F\cdot\eta}{R_u\cdot T}\right) - \exp\left(\frac{-\alpha_c\cdot F\cdot\eta}{R_u\cdot T}\right)\right] \tag{18}$$

where $i_0$ is the reference exchange current density, $C_i$ is the species concentration, $C_i^{ref}$ is the reference concentration, $\boldsymbol{\gamma}$ is an empirical concentration parameter, $\boldsymbol{\alpha}$ is the charge transfer coefficient, $\boldsymbol{F}$ is the Faraday constant, $\boldsymbol{\eta}$ is an activation overpotential, $\boldsymbol{R_u}$ is the ideal gas constant, and $\boldsymbol{T}$ is the cell temperature, respectively. Anode activation overpotential ($\eta_a$) and cathode activation overpotential ($\eta_c$) are calculated from Eqs. (19)-(20).

$$\eta_a = \varphi_s - \varphi_e \tag{19}$$

$$\eta_c = \varphi_s - \varphi_e - V_{ocv} \tag{20}$$

where $\boldsymbol{V_{ocv}}$, as calculated via the Nernst equation, is the open-circuit voltage of the cell.

$$V_{oc} = -\frac{\Delta G}{n\cdot F} + \frac{R_u\cdot T}{n\cdot F}\cdot\ln\left(\frac{a_{H_2}\cdot a_{O_2}^{0.5}}{a_{H_2O}}\right) \tag{21}$$

where $\boldsymbol{\Delta G}$ is the Gibbs free energy, $\boldsymbol{n}$ is the number of electron transport, $\boldsymbol{a}$ is the activity of species. The electron transport in gas diffusion layers and the hydrogen transport in $H_3PO_4$ doped PBI Membrane are governed by the charge conservation equation, as follows:

$$\nabla\left(-\sigma_s\cdot\nabla\phi_s\right) = 0 \tag{22}$$

$$\nabla(-\sigma_m\cdot\nabla\varphi_e) = 0 \tag{23}$$

where $\sigma_m$ is ionic conductivity. The ionic conductivity of the PBI membrane is strongly correlated with the

phosphoric acid doping level ($X$) and cell temperature ($T$) [4].

$$\sigma_m = \frac{100}{\mathrm{T}} \cdot \exp[8.0219 - (\frac{2605.6 - 70.1 \cdot \mathrm{X}}{\mathrm{T}})] \quad (24)$$

### 2.2.2 | Boundary conditions

The inlet velocities of the anode side and cathode side were calculated separately based on the stoichiometric ratio ($\lambda$), cell current ($i_{a/c}$), active surface area ($A_{MEA}$), the mole fraction of reactants ($X$), cell operating temperature ($T$), pressure ($P_{a/c}$), and gas channel area ($A_{gc}$), as shown in Eqs. (25)- (26).

$$U_{in\_anode} = \lambda_a \cdot \frac{i_a \cdot A_{MEA} \cdot X_{H_2} \cdot R_u \cdot T}{2 \cdot F \cdot P_a \cdot A_{gc}} \quad (25)$$

$$U_{in\_cathode} = \lambda_c \cdot \frac{i_c \cdot A_{MEA} \cdot X_{O_2} \cdot R_u \cdot T}{4 \cdot F \cdot P_c \cdot A_{gc}} \quad (26)$$

(i) at the anode gas flow channel inlet: $\mathrm{u} = \mathrm{u}_{\mathrm{in\_anode}}$
(ii) at the cathode gas flow channel inlet: $\mathrm{u} = \mathrm{u}_{\mathrm{in\_cathode}}$
(iii) at the anode and cathode gas flow channel outlet: $P = P_{ref}$
(iv) at the external boundaries of the cell: $\frac{\partial P}{\partial n} = 0$

When these velocities are applied to the gas flow channel inlets at the anode and cathode gas flow channel outlet, the pressure boundary condition is prescribed as $P$=$P_{ref}$. Furthermore, in order to solve the Stefan-Maxwell equations, the following conditions should be met:

(i) at the anode gas flow channel inlet: $\mathrm{w} = \mathrm{w}_{\mathrm{H2}}$
(ii) at the cathode gas flow channel inlet: $\mathrm{w} = \mathrm{wO}_2$, $\mathrm{w} = \mathrm{w}_{\mathrm{H2O}}$
(iii) at the other boundaries of the cell: $\frac{\partial c_{H_2,H_2O}}{\partial n} = 0$

The solid electrode potential and electrolyte potential equation were solved using the Dirichlet and Neumann boundary conditions. For the anode side and cathode side, reference potentials are applied along the interface between the gas flow channel and gas diffusion layer. These potentials were as follows:

(i) at the anode side: $\varphi_s = 0$,
(ii) at the cathode side: $\varphi_s = V_{oc}$
(iii) at the external boundaries of the cell: $\frac{\partial \varphi_e}{\partial n} = 0$, $\frac{\partial \varphi_s}{\partial n} = 0$

## 3 | RESULTS AND DISCUSSION

### 3.1 | Experimental results

#### 3.1.1 | Performance tests

In order to determine the exchange current density individually for each operating parameter, the performance tests for the $H_3PO_4$-doped PBI-based PEM fuel cell were carried out for six acid doping levels (4.26, 4.53, 4.95, 5.51, 7.24, 7.51 $H_3PO_4$/RPU PBI) at constant cell temperature (120 °C) and relative humidity levels (from 0 to 20% in steps of 5%). The polarization and power curves, as dependent on the relative humidity, are illustrated in Figures 1–2 for different acid doping levels at a 120 °C constant cell temperature. The figures show that the performance generally increases with the increase in the relative humidity for all acid doping levels due to the increase in the proton conductivity of the $H_3PO_4$-doped PBI membrane. Thus, it is observed that the relative humidity has a significant effect on the proton conductivity of the $H_3PO_4$-doped PBI membranes in the low relative humidity levels and the high temperature [3]. The highest power density (approximately 0.06 W $cm^{-2}$) was acquired at a 7.24 $H_3PO_4$/RPU PBI acid doping level, 20% relative humidity, and a 120 °C operating temperature.

The results of the performance tests were significantly poorer than those reported for commercial MEAs in the literature. There is a strong possibility that this poor performance was a result of the insufficient catalyst layer-ionomer interface in the used in-house MEA. Cross-sectional scanning electron microscopy (SEM) images of MEAs that have been used in the single-cell tests are shown in Figure 3. SEM images show major delamination in the membrane/electrode interface, which may severely reduce the triple-phase boundary formation, and ultimately lead to poor cell performance. Moreover, excess doping may have caused a build-up of materials, which will reduce performance drastically [21]. SEM images shown in Figure 3 confirm the presence of a build-up of materials on the MEA surface.

#### 3.1.2 | Determination of exchange current density

A zero-dimensional steady-state mathematical model was fitted to the experimental data obtained from the performance tests for various relative humidities and acid doping levels [Eq. (27)]:

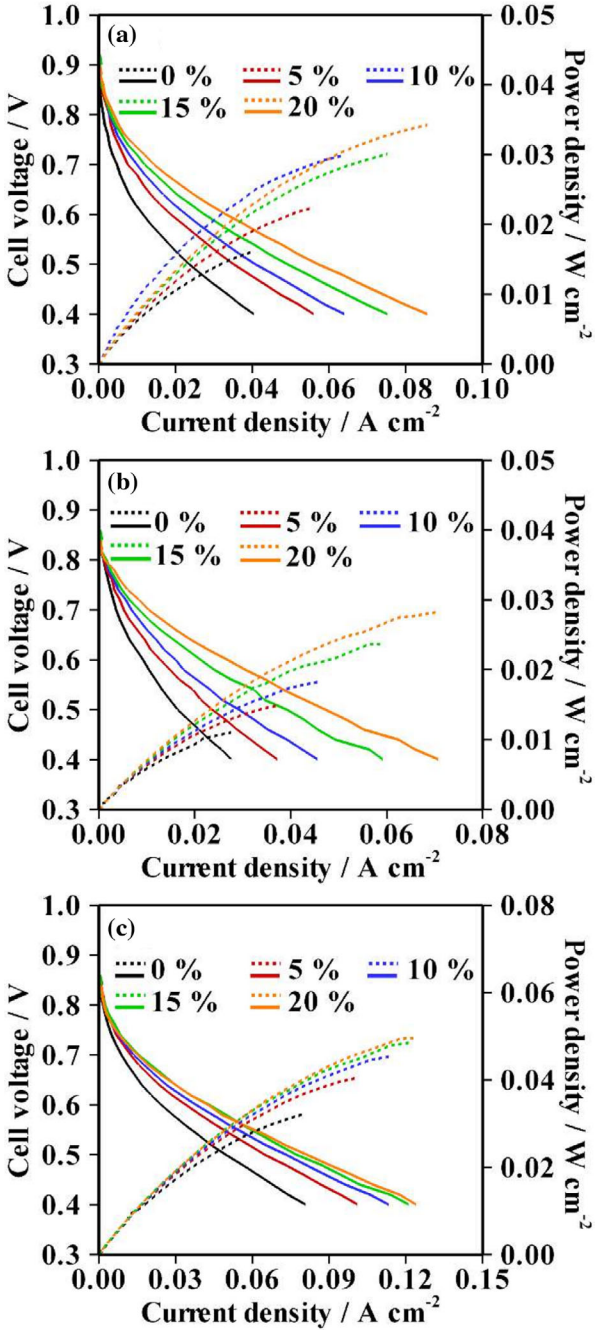


**FIGURE 1** Polarization and power curves for the different acid doping levels at 120°C [(A) X = 4.26 $H_3PO_4$/ RPU PBI; (B) X = 4.53 $H_3PO_4$/RPU PBI; (C) X = 4.95 $H_3PO_4$/ RPU PBI]

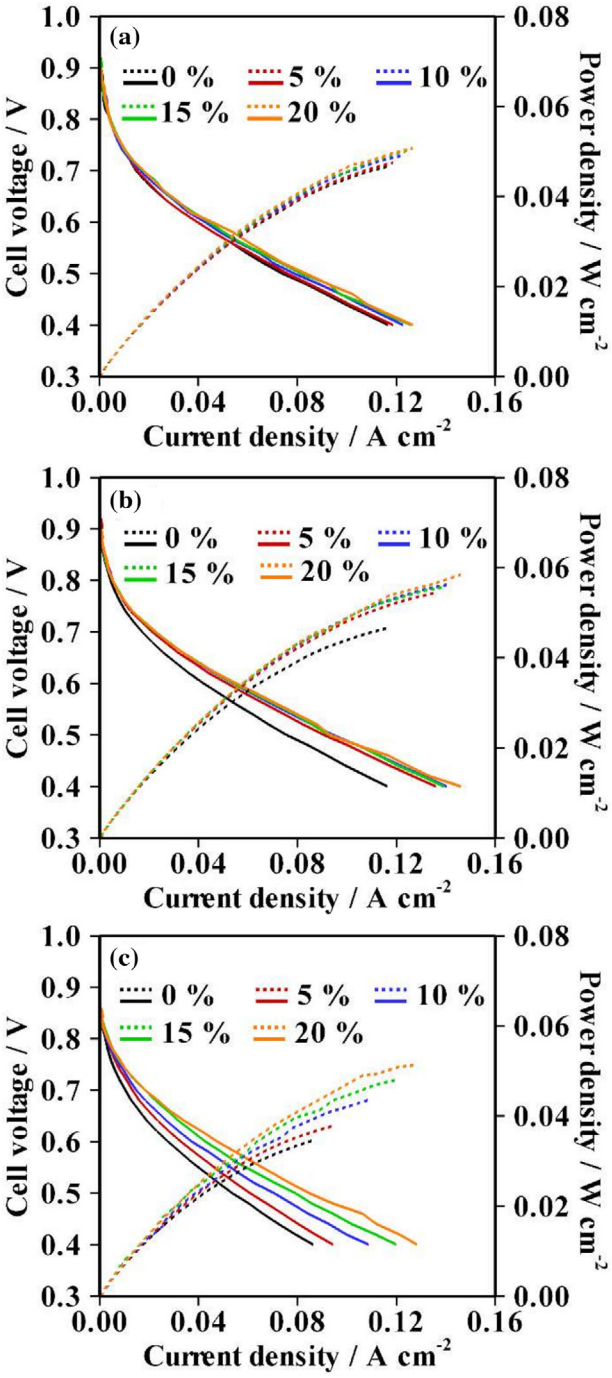


**FIGURE 2** Polarization and power curves for the different acid doping levels at 120°C [(A) X = 5.51 $H_3PO_4$/ RPU PBI; (B) X = 7.24 $H_3PO_4$/RPU PBI; (C) X = 7.51 $H_3PO_4$/ RPU PBI]

$$E_{cell} = E_0 + \frac{R_u \cdot T}{n \cdot F} \cdot \ln \frac{P_{H_2} \cdot P_{O_2}^{0.5}}{P_{H_2O}} - \frac{R_u \cdot T}{\alpha \cdot F} \cdot \ln\left(\frac{i}{i_0}\right)$$
$$-i \cdot A \cdot (\sum_{k=1}^{n} r_k) - \frac{R_u \cdot T}{n \cdot F} \cdot \ln\left(1 - \frac{i}{i_L}\right) \quad (27)$$

where $E_0$ is the maximum expected voltage, $R_u$ is the universal gas constant (8314.5 J $mol^{-1}$ $K^{-1}$), $T$ is the temperature, $n$ is the number of electrons transferred per mole of species, $F$ is the Faraday constant (96 485 C $mol^{-1}$), $P$ is the partial pressure of the species, $\alpha$ is the charge transfer coefficient, $i$ is the current density, $i_0$ is the exchange current density, $A$ is the active surface area, $r_k$ is the internal resistance, and $i_L$ is the limiting current density. The mathematical model that predicts the kinetic parameters, such as the exchange current density, charge transfer coefficient, and internal resistance, was solved using the

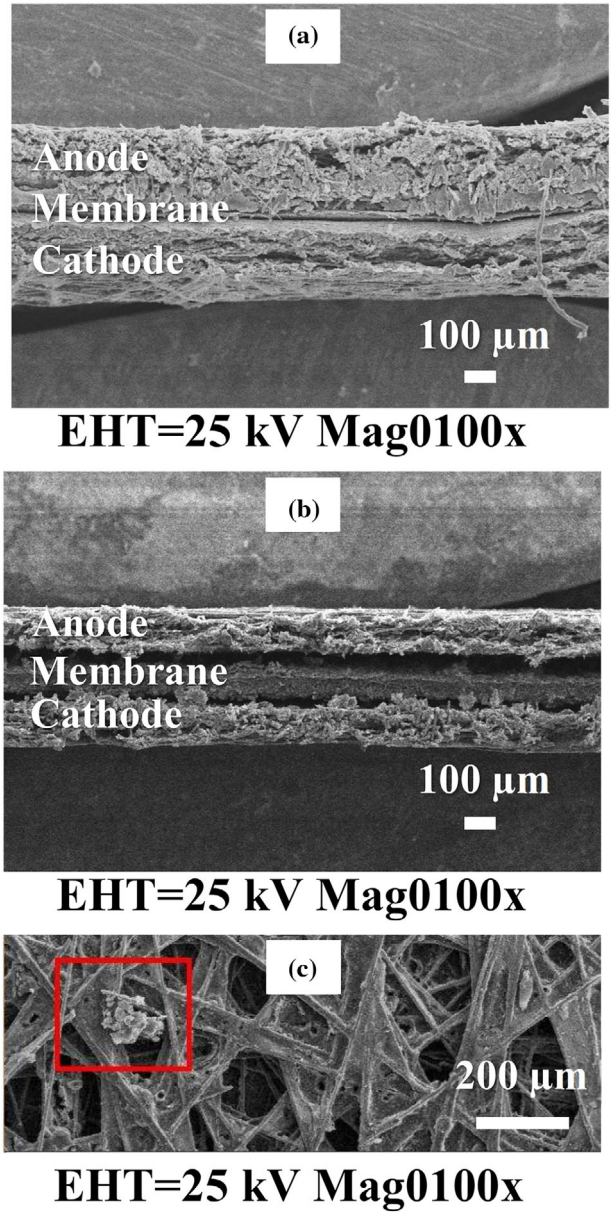


**FIGURE 3** Cross-sectional SEM images of MEAs (A) before, (B) after the single-cell tests, and (C) built-up material

MATLAB R2013a software. Because the usual exchange current densities for the anode side are negligible in comparison to the cathode side, the values obtained by the model essentially correspond to the exchange current densities for the cathode side. When the exchange current densities obtained from the model were analyzed, at all acid doping levels no major changes in the exchange current density were observed when the relative humidity was greater than 10%. Therefore, the level of relative humidity is illustrated in the range of 0% and 10% in Figure 4, which depicts the variation of the exchange current density with the acid doping level and relative humidity at constant cell temperature. The maximum exchange current density was

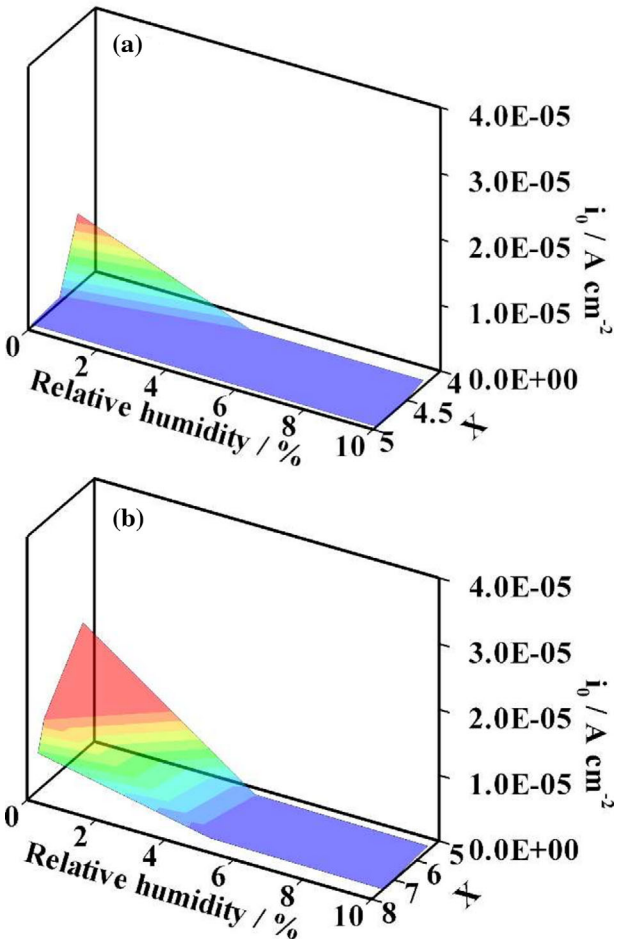


**FIGURE 4** T>he variation of the exchange current density with respect to acid doing level and relative humidity for low acid doping levels at 120°C [(A) X = 4.26, 4.53, and 4.95 $H_3PO_4$/RPU PBI, [(B) X = 5.51, 7.24, and 7.51 $H_3PO_4$/RPU PBI]

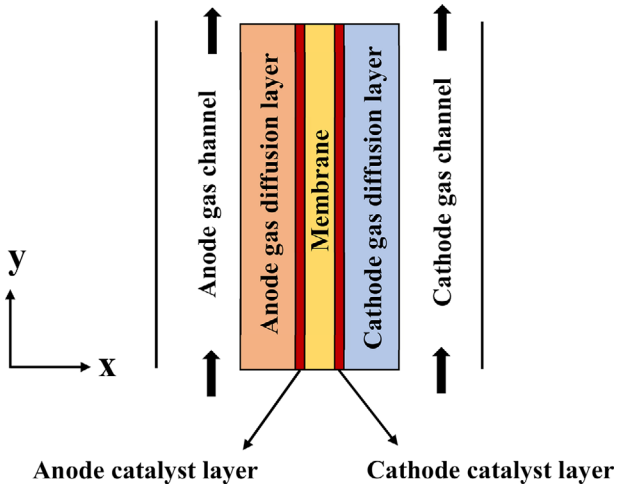


**FIGURE 5** A two-dimensional PEM fuel cell model

**TABLE 4** The results obtained for the different grid numbers at a 0.90 V cell voltage

| Grid numbers | Current density |
|---|---|
| 1710 | 0.0089007 A $cm^{-2}$ |
| 2250 | 0.00889130 A $cm^{-2}$ |
| 3150 | 0.00889006 A $cm^{-2}$ |
| 4950 | 0.00888975 A $cm^{-2}$ |
| 6750 | 0.00888969 A $cm^{-2}$ |

obtained at 0% relative humidity for 4.26 and 5.51 $H_3PO_4$/RPU PBI acid doping levels. The exchange current densities decreased with increasing acid doping level when going from 4.26 to 4.95 $H_3PO_4$/RPU PBI. The same behavior can be seen between the doping levels of 5.51 and 7.51 $H_3PO_4$/ RPU PBI. Acid doping level refers to the number of molecules of $H_3PO_4$ per repeating unit of PBI. Because of its molecular structure, every PBI repeating unit is only capable of bonding with two $H_3PO_4$ molecules. The excess amount of $H_3PO_4$ is referred to as the "free acid" and plays a role in the proton transport mechanism [21]. The reason for the exchange current density decreasing with increasing acid doping levels may be due to the increased MEA delamination and build-up of material with the increasing acid doping levels, as explained in the previous section.

## 3.2 | Numerical results

A numerical analysis was performed in order to account for the effects of acid doping level and relative humidity through exchange current density on the activation polarization in an $H_3PO_4$-doped HT-PEM fuel cell. The experimentally obtained exchange current densities were integrated into the numerical analysis since these parameters have a significant effect on activation polarization. The numerical solutions were found for the selected phosphoric acid doping level (X) (4.26, 4.95, 5.51, and 7.51 RPU $H_3PO_4$/PBI) and the different relative humidity levels (0%, 5%, and 10%) at a constant cell temperature (120 °C). First, the numerical models, having different grid numbers (1710, 2250, 3150, 4950, and 6750), were created to make the grid independent of the model results. The results obtained for these grid numbers are given in Table 4. The numerical model consists of 3150 grid numbers because the results do not change with the different grid numbers, as shown in Table 4.

The numerical data were compared with the experimental data obtained from the performance test for the same operating conditions. It can be seen that the polarization curves shown in Figure 6 are in good agreement with each other at low current density. However, the current densities obtained from the numerical study were higher

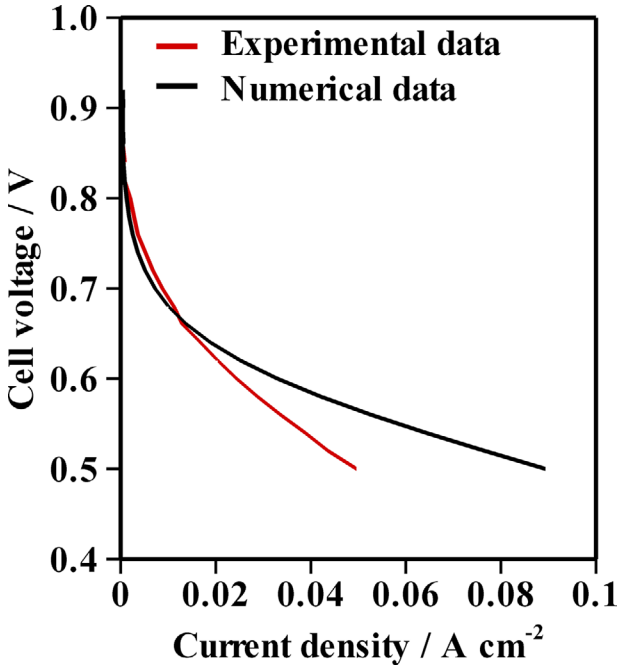


**FIGURE 6** Comparison of numerical and experimental results for X = 7.51 $H_3PO_4$/RPU PBI at $T_{cell}$ = 120 °C and RH = 5%

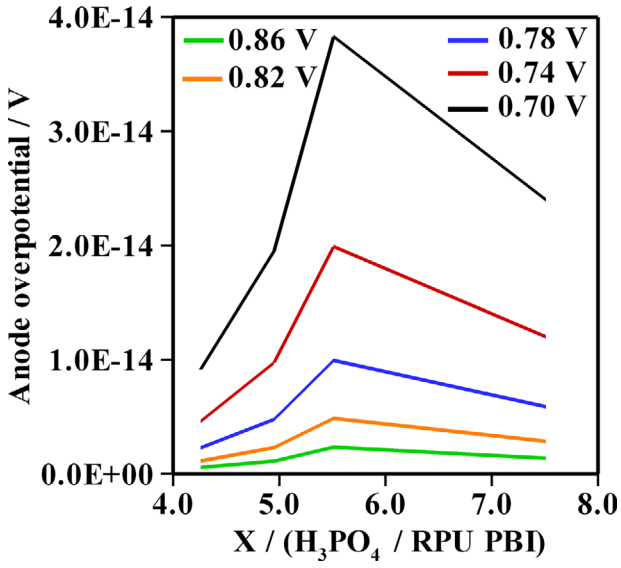


**FIGURE 7** The variation of the anode overpotential with acid doping level for the different cell voltages at 120 °C and a 0% relative humidity level

than the experimental values in the ohmic polarization region and the region with mass transport limitations of the reactants due to major delamination occurring in the membrane/electrode interface and the build-up of materials on MEA, as mentioned in Section 3.1. The numerical results presented in Figure 7 through to Figure 12 show the specific voltage ranges where activation losses are highly dominant in the polarization curve. The variation of the

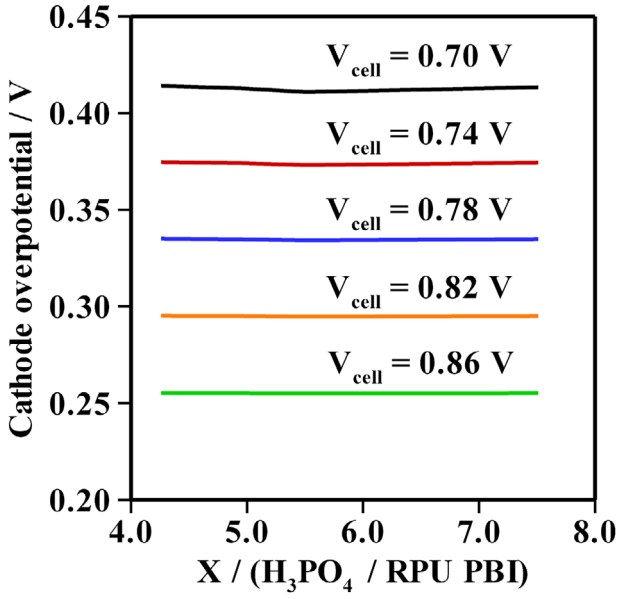


**FIGURE 8** The variation of the cathode overpotential with acid doping level for the different cell voltages at 120 °C and a 0% relative humidity level

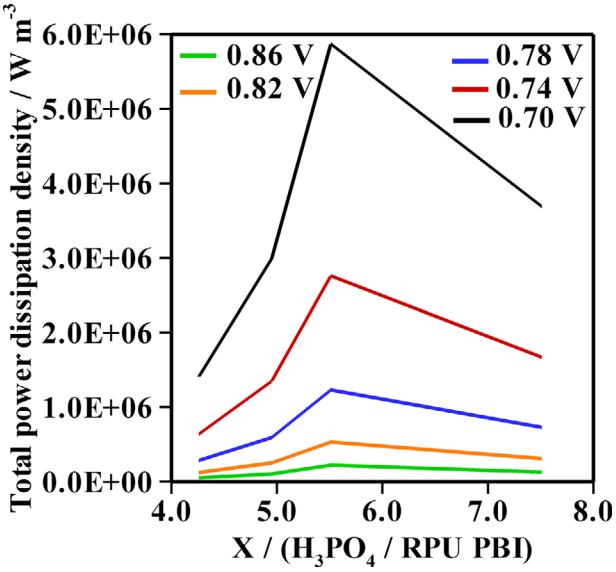


**FIGURE 9** The variations of total power dissipation density with acid doping level for the different cell voltages at 120 °C and a 0% relative humidity level

anode overpotential as dependent on acid doping level is illustrated in Figure 7 for a 0% relative humidity level and a constant cell temperature of 120 °C. As is apparent from this figure, the anode overpotential increases with decreasing cell voltage (from 0.86 V to 0.70 V) due to the change in species concentrations in the active surface area [25]. For all the cell voltages, the anode overpotential increases with increasing acid doping level, from 4.26 RPU $H_3PO_4$/PBI to 5.51 RPU $H_3PO_4$/PBI, and then decreases above the 5.51 RPU $H_3PO_4$/PBI acid doping level. The reason for this is that the potential difference, which provides ionic transfer at the membrane-electrode interface and is the source of the activation overpotential, increases with increasing ionic conductivity of the ionomer structure within the triple phase boundary due to the $H_3PO_4$-doped PBI membrane. Figure 8 shows the variation of the cathode overpotential with acid doping level for the different cell voltages at 0% relative humidity and a 120 °C cell temperature. The cathode overpotential ranges from 0.258 V to 0.415 as a result of the gradual decrease in the cell voltage from 0.86 V to 0.70 V. However, it was observed that the acid doping level of the PBI membrane has no effect on the cathode overpotential. Thus, the cathode overpotential depends on the solid potential, electrolyte potential, and cell voltage, as mentioned in Equation 15. The decrease of the exchange current density with acid doping level, as shown in Figure 4, the increase in the ionic conductivity in the PBI membrane, and the reduction of the species concentration with the cell voltage at the membrane electrode interface may have caused the cathode overpotential to remain constant. The variations of total power dissipation density with acid doping level for the different cell voltages are plotted in Figure 9 at a 0% relative humidity level and a 120 °C cell temperature. It can be seen that the power density, which is dependent on the cell current density and voltage, increases with an increase in the acid doping level from 4.26 RPU $H_3PO_4$/PBI to 5.51 RPU $H_3PO_4$/PBI, but then declines at greater than the 5.51 RPU $H_3PO_4$/PBI acid doping level for all cell voltages. It was found that the curve of total power dissipation density for both the acid doping level and cell voltage exhibits the same tendency with regard to the variation in anode overpotential because of the constant cathode overpotential. Further, this power density increases from approximately $2 \times 10^5$ W $m^{-3}$ to $6 \times 10^6$ W $m^{-3}$ with decreasing cell voltage at a 5.51 RPU $H_3PO_4$/PBI acid doping level. Figure 10 displays the variation of anode overpotential with relative humidity for a constant cell temperature of 120 °C and acid doping level (7.51 $H_3PO_4$/ RPU PBI). As can be seen in this figure, while the increase in the relative humidity from 0% to 5% causes the anode overpotential to decline linearly, the anode overpotential remains essentially constant at each cell voltage at above 5% relative humidity. It seems that the ionic conductivity of ionomer at the membrane-electrode interface is strongly affected by increasing relative humidity level, but only up to 5%. There is no change in the cathode overpotential with relative humidity as the cathode overpotential increases from 0.26 V to 0.414 V with decreasing cell voltage, as illustrated in Figure 11. It can be understood from both figures that the relative humidity at low levels (i.e., up to 5%) only has an effect on

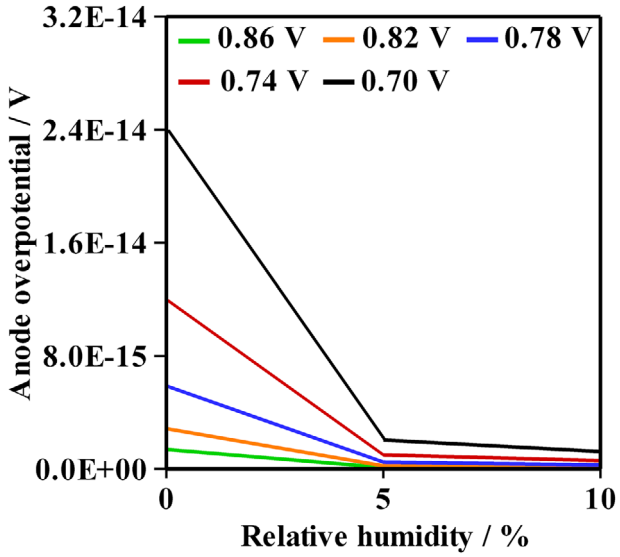


**FIGURE 10** The variation of the anode overpotential with relative humidity for the different cell voltages at 120 °C and an X = 7.51 $H_3PO_4$/RPU PBI acid doping level

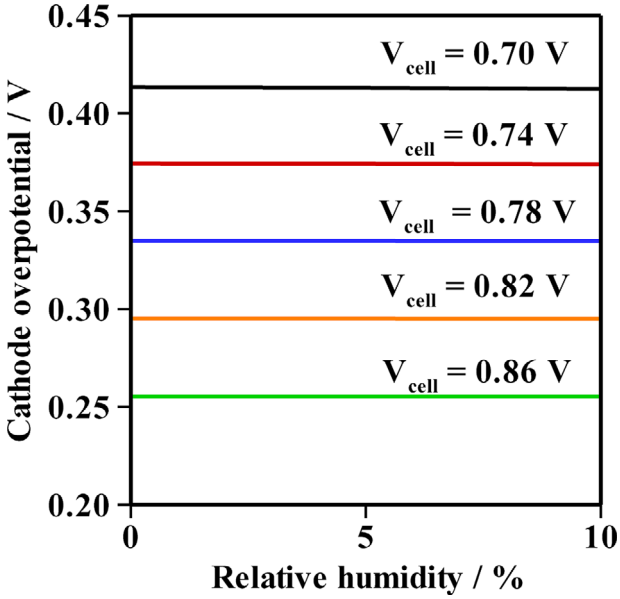


**FIGURE 11** The variation of the cathode overpotential with relative humidity for the different cell voltages at 120 °C and an X = 7.51 $H_3PO_4$/ RPU PBI acid doping level

the anode overpotential. Namely, that hydrogen splits into proton and electrons as a result of the Hydrogen Oxidation Reaction occurring at the triple-phase boundary on the anode side. Since the ionic conductivity of the ionomer is strongly dependent on the acid doping level and relative humidity causes this proton to be released and transmitted to the cathode side through the membrane, the anode overpotential is more strongly affected by the increasing acid doping level and relative humidity. The variation

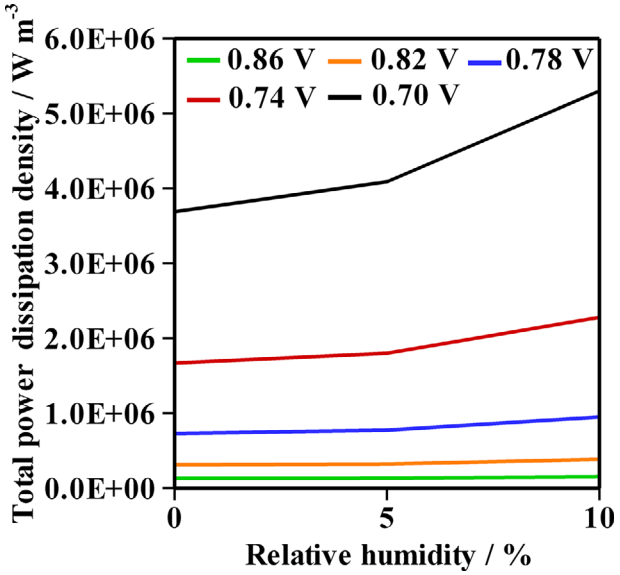


**FIGURE 12** The variation of total power dissipation density with relative humidity for the different cell voltages at 120 °C and an X = 7.51 $H_3PO_4$/ RPU PBI acid doping level

of total power dissipation density with relative humidity is presented in Figure 12 for the different cell voltages at 120 °C and a 7.51 $H_3PO_4$/ RPU PBI acid doping level. While the total power dissipation density does not change with the increase in relative humidity over a cell voltage range from 0.86 V to 0.78 V, it exhibits a slight increase at above 5% relative humidity at cell voltages of 0.74 V and 0.70 V.

## 4 | CONCLUSIONS

To reveal the effects of the exchange current density, as dependent on acid doping level and the relative humidity, on the activation polarization, the cell performance tests were first conducted at different acid doping levels and relative humidities for an $H_3PO_4$-doped PBI-based PEM fuel cell at constant cell temperature. The exchange current densities for the different acid doping levels and relative humidities were determined using the experimental data. Finally, the numerical study utilized the calculated exchange current densities to investigate the activation polarization in detail. The main conclusions obtained from this study can be summarized as follows:

It was observed that the effect of relative humidity on exchange current density was quite small at greater than 5% relative humidity for all acid doping levels, and exchange current densities decreased when increasing the acid doping level from 4.26 to 4.95 RPU $H_3PO_4$/PBI. Moreover, the same behavior was observed between doping levels of 5.51 and 7.51 RPU $H_3PO_4$/PBI. It was found

that all the overpotentials at both the anode and cathode sides and the power density increased with decreasing cell voltage according to operating conditions in the numerical study. While the anode overpotential was affected by acid doping level and relative humidity at constant cell temperature, there was almost no apparent effect of these parameters on the cathode overpotential at the same temperature. Furthermore, the maximum total power dissipation density was $6 \times 10^6$ W m$^{-3}$ at the 5.51 $H_3PO_4$/ RPU PBI acid doping level and 0.70 V cell voltage for constant cell temperature and relative humidity, whereas it exhibited a slight increase at greater than 5% relative humidities at 0.74 V and 0.70 V cell voltages for a 7.51 $H_3PO_4$/ RPU PBI acid doping level and 120 °C cell temperature.

| List of Symbols | |
|---|---|
| $C$ | Concentration / mol m$^{-3}$ |
| $D_{ij}$ | Diffusion coefficient / m$^2$ s$^{-1}$ |
| $i$ | Current density / A m$^{-2}$ |
| $m$ | Mass fraction |
| $M$ | Molar mass |
| $u$ | Velocity / m s$^{-1}$ |
| $P$ | Pressure / Pa |
| RH | Relative humidity |
| T | Temperature / K |
| X | Acid doping level |
| $\varepsilon$ | Porosity |
| $\rho$ | Density / kg m$^{-3}$ |
| $\sigma$ | Conductivity / S m$^{-1}$ |
| $\phi$ | Potential / V |
| $\eta$ | Overpotential / V |
| $\mu$ | Viscosity / kg m$^{-1}$ s$^{-1}$ |

## ACKNOWLEDGMENT

This study is supported by the Department of Scientific Research Projects at Erciyes University, project code FYL-2015-5695. They would like to thank Erciyes University for the MSc. thesis of the first author.

## REFERENCES

1. J. A. Asensio, E. M. Sánchez, P. G. Romero, *Chem. Soc. Rev.* **2010**, *39*(8), 3210.
2. A. V. Anantaraman, C. L. Gardner, *J. Electroanal. Chem.* **1996**, *414*(2), 115.
3. R. He, Q. Li, G. Xiao, N. J. Bjerrum, *J. Memb. Sci.* **2003**, *226*(1–2), 169.
4. J. A. Asensio, S. Borrós, P. Gómez-Romero, *J. Electrochem. Soc.* **2004**, *151*(2), A304.
5. Y.-L. Ma, J. S. Wainright, M. H. Litt, R. F. Savinell, *J. Electrochem. Soc.* **2004**, *151*(1), A8.
6. Y. Sun, J. Lu, L. Zhuang, *Electrochim. Acta* **2010**, *55*(3), 844.
7. D. Tang, J. Lu, L. Zhuang, P. Liu, *J. Electroanal. Chem.* **2010**, *644*(2), 144.
8. K. C. Neyerlin, W. Gu, J. Jorne, H. A. Gasteiger, *J. Electrochem. Soc* **2007**, *154*, B631.
9. Z. Liu, J. S. Wainright, M. H. Litt, R. F. Savinell, *Electrochim. Acta* **2006**, *51*(19), 3914.
10. J. Zhang, Y. Tang, C. Song, X. Cheng, J. Zhang, H. Wang, *Electrochim. Acta* **2007**, *52*(15), 5095.
11. S. Haji, *Renew. Energy* **2011**, *36*(2), 451.
12. D. Úbeda, F. J. Pinar, P. Cañizares, M. A. Rodrigo, J. Lobato, *Int. J. Hydrogen Energy* **2012**, *37*(15), 11308.
13. M. G. Santarelli, M. F. Torchio, P. Cochis, *J. Power Sources* **2006**, *159*(2), 824.
14. B. Abderezzak, *Introduction to transfer phenomena in PEM fuel cell*, Elsevier-Science, Amsterdam, Holland, **2018**, pp.186.
15. B. Carnes, N. Djilali, *J. Power Sources* **2005**, *144*(1), 83.
16. C. H. Min, Y. L. He, X. L. Liu, B. H. Yin, W. Jiang, W. Q. Tao, *J. Power Sources* **2006**, *160*(1), 374.
17. A. Iranzo, M. Muñoz, F. Rosa, J. Pino, *Int. J. Hydrogen Energy* **2010**, *35*(20), 11533.
18. D. Zhao, M. Dou, D. Zhou, F. Gao, *Int. J. Hydrogen Energy* **2016**, *41*(47), 22316.
19. M. Arif, S. C. P. Cheung, J. Andrews, *Int. J. Hydrogen Energy* **2019**, *45* (3), 2206.
20. X. W. Zhang, X. J. Wang, X. Z. Cheng, L. Jin, J. W. Zhu, T. T. Zhou, *Energy* **2020**, *207*, 118141.
21. S. Matar, A. Higier, H. Liu, *J. Power Sources* **2010**, *195*(1), 181.
22. V. Ionescu, *Ovidius University Annals of Chemistry* **2013**, *24* (1), 55.
23. S. Kim, M. Khandelwal, C. Chacko1, M. M. Mench, *J. Electrochem. Soc.* **2009**, *156* (1), B99.
24. K. M. Salahuddin, A. Nishimura, N. Oshima, L. K. Saha, *J. Thermal Sci. and Techn.* **2013**, *8* (1), 209.
25. M. M. Mench, *Fuel Cell Engines*, John Wiley & Sons, Hoboken, NJ, **2008**, pp. 168.

**How to cite this article:** M. Çelik, G. Elden. *Fuel Cells*. **2021**, *21*, 529–540.
https://doi.org/10.1002/fuce.202100035